



**HAL**  
open science

## A Metasurface Radar Monopulse Antenna

Marco Faenzi, D. Gonzalez-Ovejero, Giovanni Petraglia, Giuliana d'Alterio,  
Fabio Pascariello, Roberto Vitiello, Stefano Maci

► **To cite this version:**

Marco Faenzi, D. Gonzalez-Ovejero, Giovanni Petraglia, Giuliana d'Alterio, Fabio Pascariello, et al..  
A Metasurface Radar Monopulse Antenna. IEEE Transactions on Antennas and Propagation, 2022,  
70 (4), pp.2571-2579. 10.1109/TAP.2021.3137206 . hal-03657164

**HAL Id: hal-03657164**

**<https://hal.science/hal-03657164>**

Submitted on 9 Sep 2022

**HAL** is a multi-disciplinary open access archive for the deposit and dissemination of scientific research documents, whether they are published or not. The documents may come from teaching and research institutions in France or abroad, or from public or private research centers.

L'archive ouverte pluridisciplinaire **HAL**, est destinée au dépôt et à la diffusion de documents scientifiques de niveau recherche, publiés ou non, émanant des établissements d'enseignement et de recherche français ou étrangers, des laboratoires publics ou privés.



Distributed under a Creative Commons Attribution - NonCommercial 4.0 International License

# A Metasurface Radar Monopulse Antenna

Marco Faenzi, David González-Ovejero, *Senior Member, IEEE*, Giovanni Petraglia, Giuliana D'Alterio, Fabio Pascariello, Roberto Vitiello, and Stefano Maci, *Fellow, IEEE*

**Abstract**—This paper presents the design, fabrication and testing of a modulated metasurface antenna for monopulse radar tracking at Ka-band. The antenna consists of a circular, thin grounded dielectric layer printed by a texture of metallic patches modulated in shape and size. The patch layer can be modelled as a spatially variable capacitive impedance sheet, which together with the grounded slab contribution provides an overall, modulated, inductive boundary condition. The antenna aperture is divided into four identical angular quadrants each of them radiating independent broadside beams when excited by an individual monopole launcher. Each of the four launchers excites a TM cylindrical surface wave (SW), which is progressively converted into a leaky wave (LW) by the metasurface. The 4 sub-apertures are virtually separated by properly designing the metasurface modulation. To this end, the LW attenuation constant is calibrated for dumping sufficiently each individual SW, thus preventing the interaction between the adjacent regions. Therefore, the printed structure is not delimited by any physical separation, but only by a continuous change of the equivalent boundary conditions. The monopulse-type linearly polarized  $\Sigma$ ,  $\Delta$ ,  $\Delta_E$ ,  $\Delta_H$  beams are obtained by combining the source excitation with a simple phasing scheme. Notably, this solution does not affect the overall lightness, low profile, feed simplicity and low fabrication cost of the structure, which constitutes an inherent advantage with respect to more traditional waveguide-based solutions.

**Index Terms**—Metasurface, monopulse antenna, surface wave, leaky wave, multibeam antennas.

## I. INTRODUCTION

Monopulse radars [1] are the most used tracking systems for military applications and they are often used in space applications as well. They present advantages over alternative techniques, like those based on sequential lobes, such as robustness to the echo amplitude fluctuations and to the electronic countermeasures. The most common monopulse antennas are realized by a parabolic reflector illuminated by four horns [1], alternative solutions are reflectarrays [2], transmitarrays [3] and dielectric lenses [4]. Planar printed

phased arrays [5]-[8], slotted-waveguides or substrate-integrated slotted-waveguide arrays [9]-[13] have been also proposed to reduce the volume of the former solutions, although they often require complex distribution networks. Among low-profile monopulse antennas with a simple excitation scheme, it is worth noting radial line slot antennas (RLSAs). In [14], an annular slot-array was used to radiate sum and delta beams in the E- and H-planes by dividing the radial waveguide into four independent quadrants. A gain of 22dBi was experimentally shown for a structure with  $7.5\lambda$  radius, where  $\lambda$  is the free-space wavelength at the center frequency. In [15], the radial line structure presented a feeding scheme consisting of four probes positioned close to the center of the aperture. This antenna provided  $\Sigma$  and  $\Delta$  beams both in azimuth and elevation with a  $\Sigma/\Delta$  ratio of around 40dB. A left-handed circularly polarized (LHCP) RLSA in PCB technology at Ku-band was proposed in [16]. The antenna had a  $2.68\lambda$  radius; it was fed by a two-port microstrip Butler matrix to provide a  $\Sigma$  broadside beam with 22.2 dBi directivity and a single conical  $\Delta$  beam with maxima at  $9.4^\circ$  in elevation. A similar approach was used in [17] at W band. The resulting layout features a 4.5cm diameter aperture operating at 94GHz with a maximum directivity of 32.3dBi. Bull-eye LW antennas are also amenable for PCB implementation and they have been used to generate  $\Sigma$  and conical  $\Delta$  patterns for monopulse tracking as in [18]. The authors presented a 8.5cm radius aperture at K-band with a simulated broadside directivity around 26 dBi.

Metasurface (MTS) based antennas constitute a valid alternative to the mentioned solutions. This technology also relies on PCB technology to print subwavelength patch elements, and it has emerged in recent years as a handy, low cost and effective way to implement microwave and millimeter-wave antennas [19]. MTS structures are typically quite simple, they basically include a homogeneous electrically thin grounded slab and a top textured layer that can include several thousands of subwavelength printed metallic elements. Such elements, which shapes vary weakly in space, are arranged according to a regular lattice. Through a proper design of the top layer, the electrical properties of this kind of surfaces can be customized for a variety of microwave engineering contexts, like partially reflective surfaces [20]-[22], flat lenses [23]-[26], and planar MTS antennas [27]-[31], to mention only a few. Several textures have been proposed in [27], [28], [31]-[33] with different dimensions and shapes. They span from regular, symmetric shapes to more exotic, less symmetric ones, depending on the constraints on the

This work was supported by MBDA-Italia as part of the project “Metapulse Radar”.

M. Faenzi and S. Maci are with the Department of Information Engineering and Mathematics, University of Siena, Via Roma 56, 53100, Siena, Italy (e-mail: {faenzi, macis}@dii.unisi.it).

D. González-Ovejero is with Univ Rennes, CNRS, IETR (Institut d'Électronique et de Télécommunications de Rennes), UMR 6164, 35000 Rennes, France, (e-mail: david.gonzalez-ovejero@univ-rennes1.fr);

G. Petraglia, G. D'Alterio, F. Pascariello, and R. Vitiello are with MBDA Italia, HW Engineering Italy, via C. Calosi 1, 80070, Bacoli (NA), Italy.

isotropy/anisotropy of the equivalent boundary condition (BC).

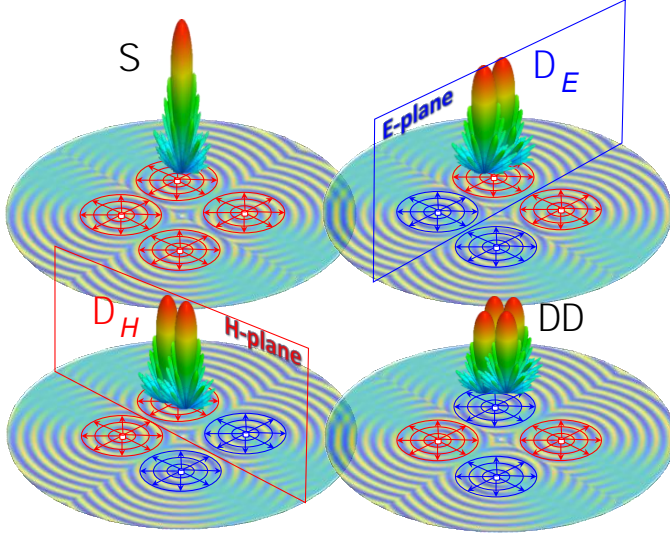


Fig. 1. The conceptual scheme of the metasurface monopulse antenna. The aperture is partitioned in four identical sub-apertures, fed by independent cylindrical surface waves. The colors on the aperture represent the impedance modulation. Four distinct beams  $\Sigma$ ,  $\Delta_E$ ,  $\Delta_H$ ,  $\Delta\Delta$  can be obtained by phased recombination of each element radiation contribution in the far field zone. The simple sources phasing scheme is represented by a colored coding for any of the four beams: sources colored in red and blue feature a zero and  $\pi$  relative phase, respectively.

In antenna applications based on surface wave (SW) excitation, MTSs usually implement periodically modulated equivalent impedance boundary conditions (IBCs). An accurate design of the modulation properties can enable a unique radiation pattern control. The radiation phenomenon is based on translating one Floquet mode spectral footprint within the visible range. This way, the dominant  $TM_0$  mode is transformed into a leaky wave (LW) that gradually converts the SW power density into radiated power intensity [33], [34]. By appropriately tailoring the IBC modulation features, one may control the phase, polarization and amplitude of the -1 indexed Floquet mode independently, leading to highly customizable apertures. Remarkably, IBCs design simply translates into engineering the texture's geometrical properties without altering the overall low profile, low mass, low cost and simplicity of the feeding scheme. In this regard, MTS antennas appear as a prominent technology for several applications, especially for space and satellite communications, where light and flat apertures are requested.

The inherent advantages of MTS technology have driven considerable research efforts for the development of modulated planar antennas able to provide high efficiency [31], [33], [34] large bandwidths [35], [36], contoured beams and multi frequency operability [31], multiple beams [37], [38] (the latter approach is based on a quasi-direct aperture synthesis method [39]) or dual polarization [40].

In this paper, we have designed and realized a modulated MTS antenna for monopulse radar applications at Ka-band. The aperture proposed in this work consists of a circular domain divided into four identical angular sectors, each one illuminated by a phased monopole (Fig. 1). Each of the four

sub-apertures is capable of radiating a linearly polarized broadside beam. A linearly polarized single-fed antenna, based on aperture partition, was also obtained in [41]. Differently from that design, we use aperture partition to obtain a set of distinct beams; however, here the individual partition is designed directly to get linear polarization. The phased recombination of the four radiated beams allows one to generate four distinct patterns, i.e.: a sum pattern ( $\Sigma$ ), a delta-azimuth pattern ( $\Delta_E$ ), a delta-elevation pattern ( $\Delta_H$ ), and a delta-delta pattern ( $\Delta\Delta$ ) (see Fig.1). The  $\Delta_E$  and  $\Delta_H$  patterns have maxima aligned in azimuth along  $\phi=45^\circ$  and  $\phi=135^\circ$ , respectively; and the  $\Delta\Delta$  pattern features four maxima aligned along  $\phi=0^\circ$  and  $\phi=90^\circ$ . The four sub-apertures are virtually separated by properly designing the MTS modulation. To this end, the LW attenuation constant is calibrated for damping sufficiently each individual SW thus preventing the interaction with the adjacent regions. Therefore, the printed structure is not delimited by any physical separation, but only by a continuous change of the equivalent boundary conditions.

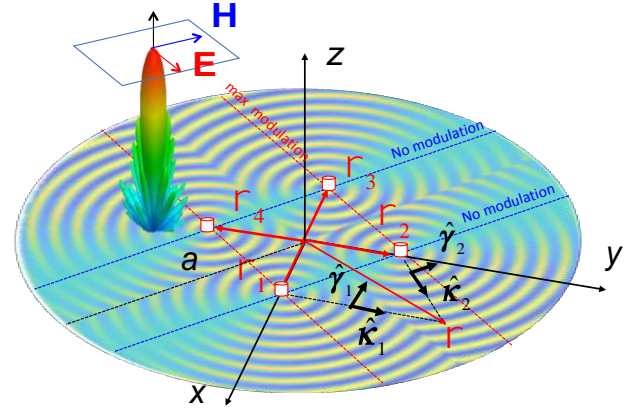


Fig. 2 Geometry of the problem. A global reference system has the origin at the center of the circular aperture of radius  $a$ . The aperture is defined by a set of four local reference coordinate systems centered in each monopole source, placed at  $\rho_i$  in the global system. Each local coordinate system is characterized by cylindrical coordinate unit vectors  $(\hat{\mathbf{k}}_n, \hat{\boldsymbol{\gamma}}_n)$ ,  $n=1, \dots, 4$ . The colored map represents the TM-TM component of the tensor  $\underline{\underline{\chi}}$ ; the dotted red and blue dashed lines on the aperture show the directions of maximum modulation and no-modulation of the above mentioned impedance component. The pattern in the inset shows the E and H plane of the antenna.

## II. METASURFACE DESIGN

The monopulse antenna is constituted by a grounded dielectric layer of circular shape, on top of which a thin texture of subwavelength printed metal elements imposes a sheet transition IBC [33] given by

$$\mathbf{E}_t = j \underline{\underline{\mathbf{X}}} \cdot \hat{\mathbf{z}} \times \left[ \mathbf{H}_t|_{z=0^+} - \mathbf{H}_t|_{z=0^-} \right] \quad (1)$$

where the reactance contribution provided by the elements is represented by the tensor  $\underline{\underline{\mathbf{X}}}$ , and the averaged tangential electric field  $\mathbf{E}_t$  is proportional to the magnetic field

discontinuity  $\mathbf{H}_t|_{z=0^+} - \mathbf{H}_t|_{z=0^-}$  measured closely above and below the texture layer. The circular aperture has radius  $a=7.5\text{cm}$  and its area is divided into four sub apertures consisting of identical angular regions. A local reactance tensor  $\underline{\underline{X}}_n U_n$ , where  $n=1, \dots, 4$ , is defined on each angular region using its local coordinate system as reference; unit vectors  $(\hat{\boldsymbol{\kappa}}_n, \hat{\boldsymbol{\gamma}}_n)$  that are centered on the local feed position (see Fig.2) are used to describe the four local systems.

The unit vectors  $\hat{\boldsymbol{\kappa}}_n, \hat{\boldsymbol{\gamma}}_n$  are defined as  $\hat{\boldsymbol{\kappa}}_n = (\boldsymbol{\rho} - \boldsymbol{\rho}_n) / R_n$  and  $\hat{\boldsymbol{\gamma}}_n = \hat{\boldsymbol{z}} \times \hat{\boldsymbol{\kappa}}_n$ , where  $R_n = |\boldsymbol{\rho} - \boldsymbol{\rho}_n|$ ;  $\boldsymbol{\rho}$  is a generic position on the aperture with respect to the global reference system and  $\boldsymbol{\rho}_n$  represents the positions vector of the local feeds with respect to the same reference system.  $U_n$  is an angular unit step function defined on the  $n$ th angular region as  $U_n = 1$  on  $-\pi/4 + (n-1)\pi/2 < \phi \leq \pi/4 + (n-1)\pi/2$  for  $n=1, \dots, 4$  and for  $0 < \rho < a$  and  $U_n = 0$  elsewhere, with  $\phi$  and  $\rho$  being the azimuthal and radial coordinate of the global reference system respectively (see Fig.2). Therefore, the reactance tensor  $\underline{\underline{X}}$  for the global aperture can be written as

$$\begin{aligned} \underline{\underline{X}} &= \sum_{n=1}^4 \underline{\underline{X}}_n U_n = \\ &= \sum_{n=1}^4 \left[ \hat{\boldsymbol{\kappa}}_n \hat{\boldsymbol{\kappa}}_n X_{\kappa\kappa,n} + (\hat{\boldsymbol{\kappa}}_n \hat{\boldsymbol{\gamma}}_n + \hat{\boldsymbol{\gamma}}_n \hat{\boldsymbol{\kappa}}_n) X_{\kappa\gamma,n} + \hat{\boldsymbol{\gamma}}_n \hat{\boldsymbol{\gamma}}_n X_{\gamma\gamma,n} \right] U_n. \end{aligned} \quad (2)$$

We note that the entries  $X_{\chi\chi,n}$  in (2), where the subscript  $\chi$  stands both for  $\kappa$  and  $\gamma$ , are sinusoidally modulated functions characterized by a modulation index  $m_\chi$ , period  $d$  and  $n$ -independent average reactance  $\bar{X}$  [30]. Each of the four angular regions represented in Fig.2 are designed to provide a linearly polarized broadside beam, which copolar field component is oriented along  $\phi=45^\circ$  (see Fig.2). Once the modulation parameters and the positions of the sources  $\boldsymbol{\rho}_n$  are defined, the global reactance tensor  $\underline{\underline{X}}$  is obtained from (2). As a reference, the TM-TM component of  $\underline{\underline{X}}$  is pictorially represented in Fig.2. The choice of  $\boldsymbol{\rho}_n$  in multipoint fed MTS apertures is quite important since it affects the pattern shape. On the other hand, the  $\Sigma$ ,  $\Delta_E$ ,  $\Delta_H$  and  $\Delta\Delta$  beams are obtained by linear superposition of the patterns originated by any angular region alone. Each individual angular region is illuminated by a SW launcher that provides either an incident field in phase or with a  $\pi$  relative phase with respect to the other feed points. Therefore, the source phasing determines the overall antenna radiation pattern, which is obtained by adding the radiation patterns relevant to each angular region weighted by  $\pm \exp(jk\hat{\boldsymbol{\kappa}} \cdot \boldsymbol{\rho}_n)$ , where the sign of the exponential function depends on the phasing of each of the incident fields and  $k$  is the free space wavenumber at the center frequency  $f_0$ . On the other hand, the relative distance between the sources determines the ports' mutual coupling. The coupling between the sub-apertures is due to the residual fraction of the SW

traveling from the source point  $\boldsymbol{\rho}_i$  to source point  $\boldsymbol{\rho}_j$  (see Fig.2). This fraction is proportional to the factor  $\exp(-\alpha|\boldsymbol{\rho} - \boldsymbol{\rho}_n|)$ , with  $\alpha$  being the LW attenuation parameter. For constant  $\alpha$ , increasing mutual ports decoupling would lead to an increase of the value  $|\boldsymbol{\rho}_n|$ , that is, to move feeding points towards the rim of the aperture. Conversely, edge diffraction is minimized only if a sufficient distance  $|a - \boldsymbol{\rho}_n|$  is preserved. Conciliating these two conflicting requirements leads to a trade-off in the choice for the feeds position, which in the present design is fixed to  $|\boldsymbol{\rho}_n| = 3\lambda_0$  for any  $n$ , where  $\lambda_0$  is the free space wavelength at  $f_0$ . Thus, the four feeding points are placed at  $\boldsymbol{\rho}_n = \pm 3\lambda_0 \hat{\boldsymbol{x}}$  for  $n=1,3$  and at  $\boldsymbol{\rho}_n = \pm 3\lambda_0 \hat{\boldsymbol{y}}$  for  $n=2,4$ .

The modulated IBC is designed on a Rogers RO3006 laminate characterized by permittivity  $\epsilon_r=6.15$  and thickness  $h=0.635\text{mm}$ . The average transparent reactance is chosen equal to  $\bar{X} = -290\Omega$ . The solution of the MTS dispersion equation [42] brings one to find the wavenumber  $\beta_{sw}$  that characterizes the SW propagating on the homogeneous (non-modulated) surface. For a broadside beam the modulation periodicity is defined as  $d=2\pi/\beta_{sw}$ , and in the case treated here assumes a value  $d \cong 6\text{mm}$ . The expressions of the modulation indexes  $m_\kappa$  and  $m_\gamma$  (respectively associated to the reactance tensor entries  $X_{\kappa\kappa,n}$  and  $X_{\gamma\gamma,n}$  and to  $X_{\kappa\gamma,n}$  and  $X_{\gamma\kappa,n}$ ) take the form

$$\begin{aligned} X_{\kappa\kappa,n} &= \bar{X} \left[ 1 + m_{\kappa,n} \sin(\beta_{sw} \kappa_n - \gamma_n) \right] \\ X_{\kappa\gamma,n} &= \bar{X} \left[ m_{\gamma,n} \sin(\beta_{sw} \kappa_n - \gamma_n) \right] \\ X_{\gamma\gamma,n} &= \bar{X} \left[ 1 - m_{\kappa,n} \sin(\beta_{sw} \kappa_n - \gamma_n) \right] \end{aligned} \quad (3)$$

where  $m_\kappa = m_0 [\cos \gamma \ \sin \gamma]$  and  $m_\gamma = m_0 [\cos \gamma \ \sin \gamma]$ , while  $m_0$  is constant, chosen equal to  $m_0=0.25$ . The TM-TM reactance function is designed in such a way that the maximum and zero modulation values are found at  $+45^\circ$  and  $-45^\circ$  of the local azimuth angle, respectively. This implies a linear polarization of the E-field at  $45^\circ$  (see Fig. 2). This is imposed, according with [30], by considering that the -1 indexed TM Floquet mode is polarized along the direction  $(\hat{\boldsymbol{x}} + \hat{\boldsymbol{y}})$ . Once the tensor  $\underline{\underline{X}}$  is completely characterized, the solution of the local canonical problem [43] that models the so defined reactance modulation provides the LW attenuation factor, which assumes the value  $\alpha=2.64\text{m}^{-1}$ . A simple estimation of the SW propagation decay  $\tau$  on circular domains is easily derived [30] and reads

$$= \left( |\boldsymbol{\rho} - \boldsymbol{\rho}_n| \right)^{1/2} \exp \left[ -\alpha \left( |\boldsymbol{\rho} - \boldsymbol{\rho}_n| \right) \right]_{\text{dB}} \quad (4)$$

from (4) we obtain  $\tau_r = -13.7\text{dB}$  and  $\tau_r = -12.3\text{dB}$  respectively for SW decay along the shortest feed-to-feed path and along the shortest feed-to-rim path. According to this estimation, the choice adopted for feeds positioning is considered to be suitable to provide sufficient ports decoupling, devised a posteriori being at a level of  $-30\text{dB}$ .

### III. NUMERICAL ANALYSIS

The aperture detailed in the previous section has been implemented by printed metal elements for numerical validation by a FMM approach and successive fabrication and testing. To this end, the modulated reactance functions given by (3) are sampled by several thousands of unit cells on a cartesian grid with periodicity  $p=1.1$  mm and implemented by elliptically shaped patches [32]. This kind of elements is efficiently described by entire domain analytical basis functions [32], which significantly help to reduce the time to compute the associated reactance by a periodic spectral MoM solver [44]. The aperture synthesis relies on the preliminary construction of a reactance database that links the main geometrical parameters of the patch elements with the corresponding impedance tensor. Usually, to speed up the database construction only a few element geometries are analysed to obtain the corresponding anisotropic reactances. Next, the obtained database is interpolated to produce a denser mapping. The aperture reactance described by (2), (3), with average reactance, modulation index and periodicity provided in section II is then sampled according to a cartesian grid characterized by the lattice periodicity  $p$ . In other words, one associates a local reactance value to each of the so defined unit cells on the antenna aperture. Every square unit cell hosts an elliptically shaped patch element [32]; the element synthesis, done cell by cell, is performed by minimizing the least square error (LSE) between the local reactance tensor and the anisotropic reactances in the database that has been preliminarily evaluated.

Radiation coming from each excited source has been tested first and compared using two in-house developed full-wave solvers. The first solver represents the reactance function in (3) as a continuous ideal IBC in a method of moments (MoM) framework. It provides a fast solution, owing to the use of Gaussian-Ring basis functions [45]. The second method is based on a fast multipole method (FMM) analysis of the structure implemented by elliptical patches [31]. However, the two solvers include both a vertical substrate-embedded monopole as SW launcher.

The embedded element pattern (EEP) calculated by the IBC-MoM and FMM, relevant to each individual source, have thus been calculated by positioning one monopole at a time in absence of the others (the CAD layout of the real feed is instead shown in the top-right inset of Fig. 7). The EEPs are represented by the plots in Fig.3(a)-(d) that show the copolar and cross polar components on a pattern cut along  $\phi=45^\circ$ . One notices in Fig.3 that, for any of the four angular regions, an excellent agreement is obtained between co and crosspolar components calculated with the IBC-MoM and the FMM analysis.

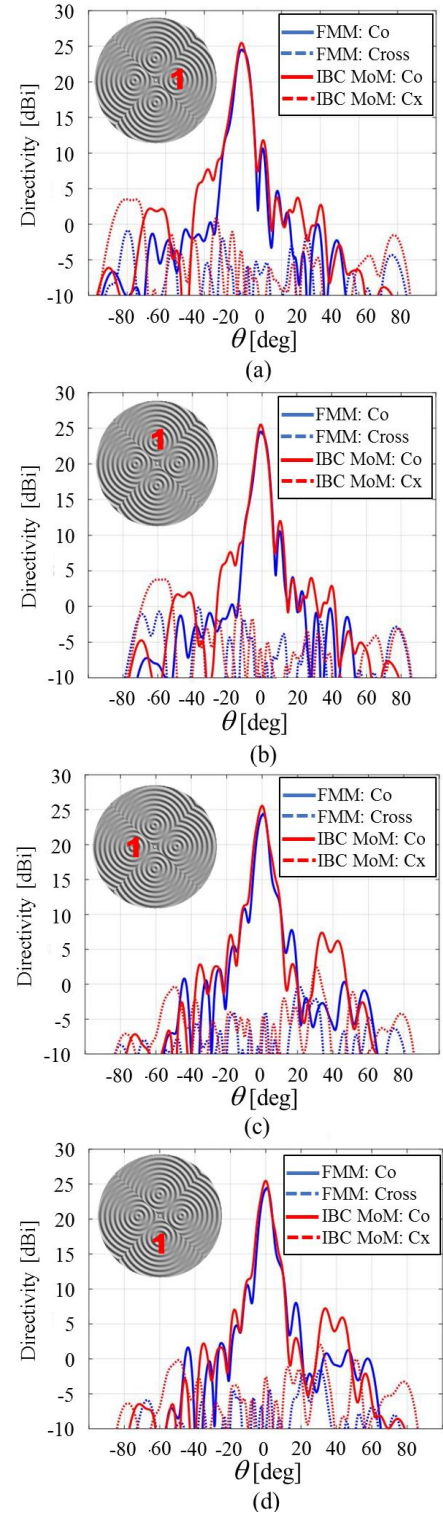


Fig. 3 The radiation of each sub-aperture has been computed using two different full-wave solvers. The first solver uses an ideal continuous representation of the reactance in a MoM framework [45], the second one is based on a FMM analysis [31] of the textured aperture. Each sub-aperture is excited by an elementary vertical monopole while other feeds are left switched off. In the sub-figures, the label “1” indicates the feed from which the SW is excited. The co and cross-polar directivity patterns computed with the IBC-MoM and FMM are compared in (a), (b), (c), and (d) when sources 1, 2, 3 and 4, respectively, are active, while the other ones are switched off (as shown in the insets). Directivity patterns are calculated along the cut  $\phi=45^\circ$ .

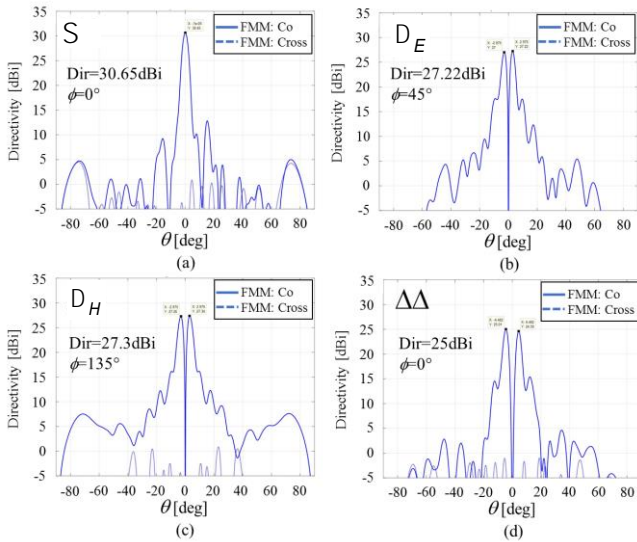


Fig. 4 (a)  $\Sigma$ , (b)  $\Delta_E$ , (c)  $\Delta_H$ , and (d)  $\Delta\Delta$  directivity patterns, calculated from the FMM, results by combining the four EEPs. Patterns are evaluated along the cuts containing the maxima, at the azimuthal angles written on the top left corner of each frame; the values of the obtained peak-directivities are also written inside each picture.

Also, the four EEPs are sharp broadside beams, with quite low levels (20 dB below the main beam maximum) of the cross polar components. The embedded element patterns are next used to reconstruct the four  $\Sigma$ ,  $\Delta_E$ ,  $\Delta_H$ ,  $\Delta\Delta$  beams according to the feeding scheme represented in Fig.1. Indeed, as graphically displayed in Fig.1, we recombine the four EEP contributions by considering a relative phase term  $\Delta\phi=0$  for the sources colored in red and  $\Delta\phi=\pi$  for sources colored in blue. All the four patterns, obtained by the FMM solver, are shown in Fig.4(a)-(d). Each beam is shown along the azimuthal direction that contains the pattern maximum (see Fig.4). For any of the beams in Fig. 4(a)-(d), one can observe a very low level of the cross-polar components, which are always 25dB below the pattern maximum.

Besides, sharp copolar beams are predicted. In particular, the peak directivity of the  $\Sigma$  beam is around 30.6dBi, SLLs relevant to  $\Delta_E$ ,  $\Delta_H$  and  $\Delta\Delta$  beams are lower than -10dB and deep pattern nulls at broadside are obtained.

Fig.5 represents the four copolar patterns maps, calculated by the IBC-MoM, in the  $u$ - $v$  plane. It can be easily noticed that a very good pattern symmetry is obtained for any beam generated by the sub-aperture partitioning method. A precise alignment of the  $\Delta_E$ ,  $\Delta_H$ ,  $\Delta\Delta$  beams maxima is obtained along  $\phi=45^\circ$ ,  $\phi=135^\circ$  and  $\phi=0^\circ$ ,  $90^\circ$ , respectively, whereas resolution angles of the  $\Delta_E$  and  $\Delta_H$  beams are both around  $6^\circ$ . The resolution angle of the  $\Delta\Delta$  beam is instead around  $8^\circ$ .

Fig. 6 shows the scattering parameters involving port 1 calculated by the commercial software CST Microwave Studio [46] compared to the measured ones. In Fig.6, one can notice a quite good agreement between experiment and simulations results. The parameters involving the other ports are almost identical (in the limit of the numerical description and instrumental sensitivity) because of the symmetry of the structure. It is seen, in particular, that the level of decoupling

between any of the feed ports is of the order of -30dB.

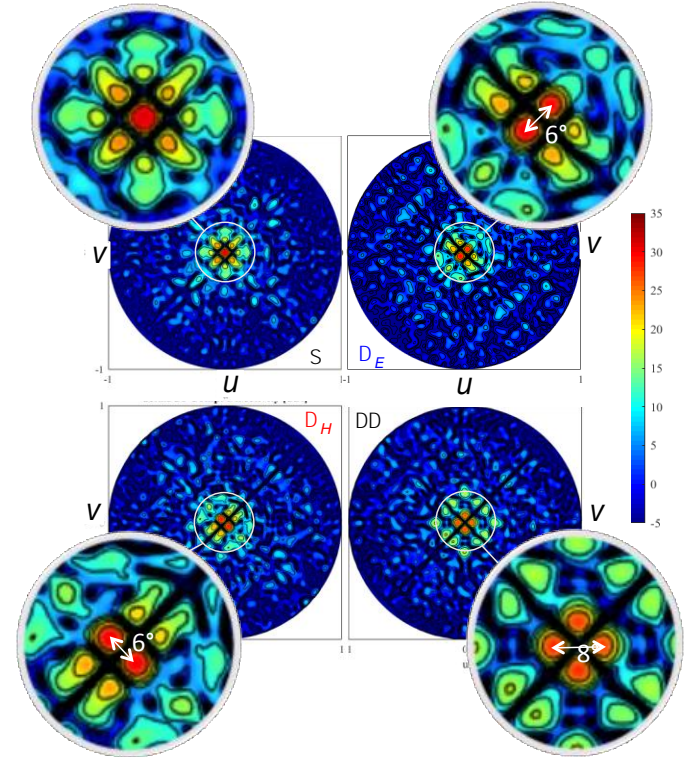


Fig. 5. Spectral  $u$ - $v$  maps (copolar component) of the four monopulse beams, with zooms of the angular region  $\pm 18^\circ$  around broadside. Results are obtained by using the IBC-MoM solver [45].

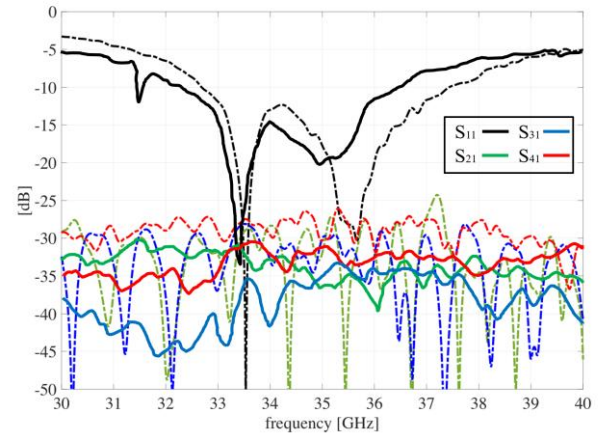


Fig. 6.  $S$ -parameters for port 1: the solid lines show the measured  $S_{ij}$  coefficients, while dashed ones report the  $S$ -parameters calculated by the commercial software CST Microwave Studio [46].

#### IV. IMPLEMENTATION AND MEASUREMENTS

The aperture described in the previous sections has then been fabricated and tested. Fig. 7 shows a photo of the prototype. The insets show the feeding points of the prototype, which include the inner conductor of a standard coaxial cable surrounded by a printed metal ring that serves for impedance matching purposes. A zoom of the CAD model used for the scattering matrix results presented in Section III is also shown. As already mentioned, the elements have been printed on a substrate Rogers RO3006 characterized by permittivity

$\epsilon_r=6.15$  and thickness  $h=0.635\text{mm}$ . The measurements have been performed in the near-field chamber of MBDA Italy. Fig. 8(a) presents the measured pattern in the  $\theta$ - $\phi$  plane at 33.5GHz when the source at  $\rho_2$  is excited while the other ones are switched off and terminated with a matched load. Figs. 8(b)-(e) show instead comparisons between normalized calculated and measured normalized directivity patterns for the  $\Sigma$ ,  $\Delta_E$ ,  $\Delta_H$  and  $\Delta\Delta$  beams, respectively;  $\Sigma$  and  $\Delta\Delta$  beams are plotted along  $\phi=0^\circ$ , while the  $\Delta_E$  and  $\Delta_H$  patterns are shown in the antenna E and H planes, respectively. All patterns have been normalized to their maxima; the relative levels with respect to the maximum of the  $\Sigma$  pattern are -3dB for the  $\Delta_E$ ,  $\Delta_H$  beams, and -6dB for the  $\Delta\Delta$  beam. The numerical results are calculated by the FMM-MoM analysis [31]. Overall, the agreement between experimental and numerical results can be considered satisfactory; the measured beamwidth for the  $\Sigma$  beam is quite consistent with respect to the FMM prediction, while the measured SLL settles 15 dB below the pattern maximum. A good agreement between experimental and simulation results is also shown in Figs. 8(c), (d) for the  $\Delta_E$ ,  $\Delta_H$  patterns. Small asymmetries of the two specular beams characterizing the  $\Delta_E$ ,  $\Delta_H$  patterns appear in the measurements, such asymmetry is more evident in the  $\Delta_E$  pattern. This effect is due to a small misalignment in the measurement setup, which leads to a near field sampling on a slightly tilted azimuthal cut with respect to the E-plane (relevantly to the  $\Delta_E$  beam in Fig. 8(c)). When this occurs, one or both of the specular beams experience a decrease of the pattern maximum and a beamwidth narrowing, an effect that can be noticed in Fig.8(c). Some discrepancies between measured and predicted patterns are also observed in Fig. 8(e) for the  $\Delta\Delta$  beam. In this case, the modification of the pattern shape is mainly due to an imperfect relative phasing of the sources by the feeding network. Such non-ideality mainly affects the array factor shape, which for the  $\Delta\Delta$  beam should show a deep null at boresight (around -45dB with respect to the pattern maxima) as displayed by the FMM prediction (blue curve in Fig.8(e)). This null tends instead to increase if the array factor terms do not add up in the far region with the proper phase. This effect can be observed in Fig.8(e), where the measured null at broadside is only around 22dB below the pattern maxima.

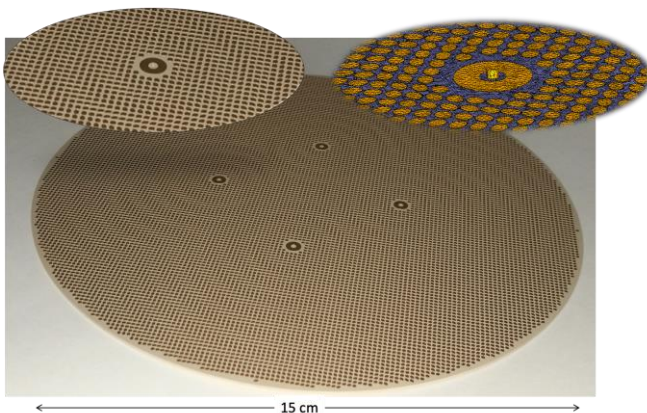
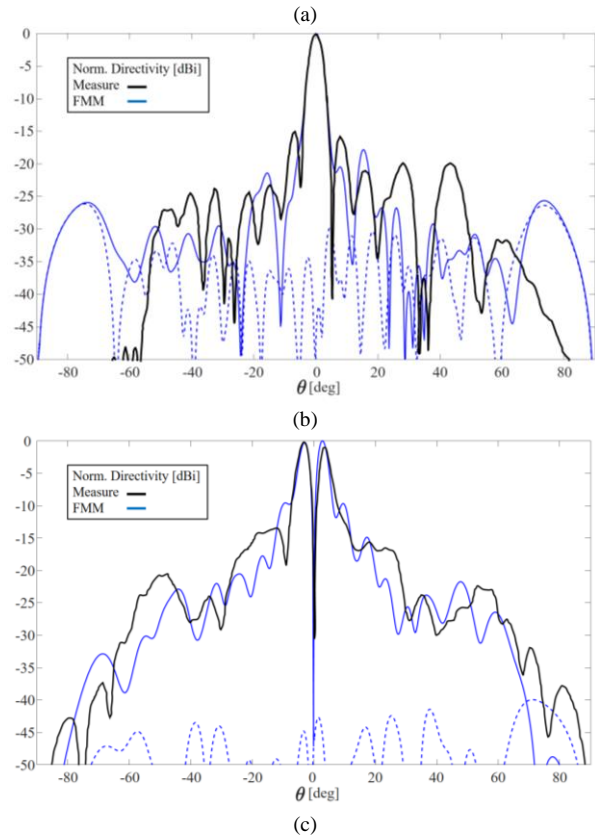
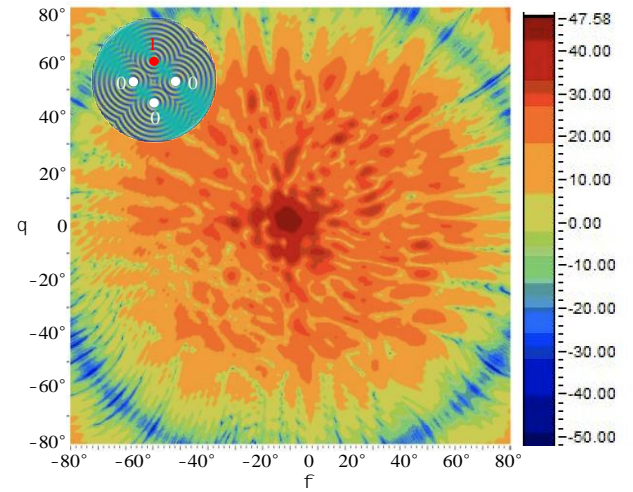


Fig.7 Pictures of the fabricated monopulse prototype. The entire aperture is represented in the bottom picture, where the four embedded feed points are visible. The insets show details of the feeding structure. In particular the top right picture shows a detail of the CAD model with the slightly protruding coaxial pin.



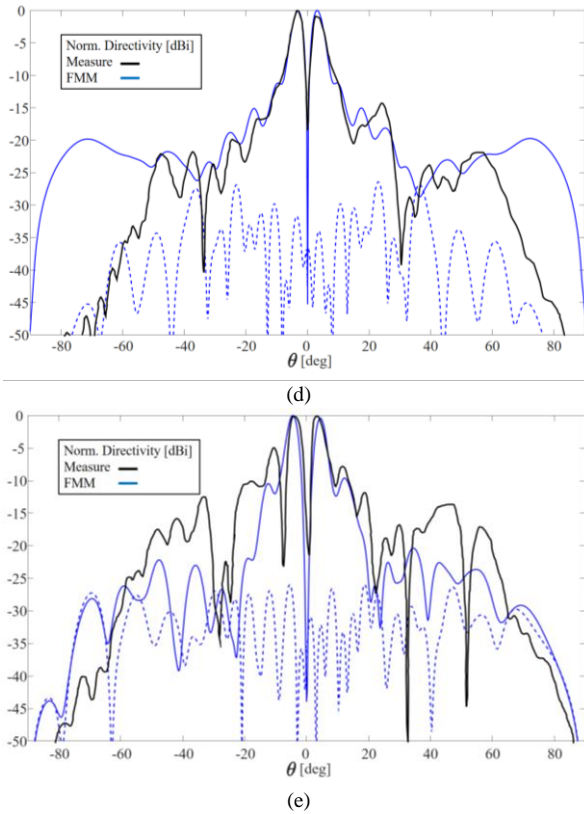


Fig. 8 Calculated and measured patterns of the monopulse antenna at 33.5 GHz. (a) Beam relevant to source n.2 in the  $\theta$ - $\phi$  plane. Comparison between normalized directivities for: (b) the  $\Sigma$  beam in the  $\phi=0^\circ$  plane, (c) the  $\Delta_E$  beam in the  $\phi=45^\circ$  plane, (d) the  $\Delta_H$  beam in the  $\phi=135^\circ$  plane, and (e) the  $\Delta_\Delta$  beam in the  $\phi=0^\circ$  plane. The solid black curves stand for the measured results, while the solid and dashed blue lines correspond to the co- and cross-polar patterns calculated by an in-house developed FMM-MoM solver [31].

Table I shows the measured antenna parameters at 33.5 GHz. The coupling coefficients among the ports (not reported here) are of the order of -30 dB, with an input return loss of about 25 dB for each port. The coupling between ports  $i$  and  $j$  (with  $i \neq j$ ) can be estimated from the feed to feed decay in (4). The closest feeds are placed at a distance  $\rho_f = 3\lambda_0$  (25.7mm) and each feeding annular patch (shown in the insets of Fig.7) has outer radius  $r_f = 1.8924$ mm. Therefore, the angle of capture of the cylindrical-wave launched by feed  $i$  at feed  $j$  is  $\phi = 0.147$ rad, and the captured power  $P_{captured}^{(j)}$  is

$$P_{captured}^{(j)} = \left. \begin{matrix} (i) \\ sw \end{matrix} \frac{\rho_0 e^{-2\alpha\rho_f}}{\rho_f e^{-2\alpha\rho_0}} \frac{\phi}{2\pi} \right|_{dB} \quad (5)$$

where  $\rho_0 = 0.3048$ mm is the radius of the coaxial inner conductor in the excited feed and  $P_{sw}^{(i)}$  is the surface wave power launched by feed  $i$ , that may be considered unitary. Since  $e^{-2\alpha\rho_f}|_{dB} = -13.7$  dB, we obtain with the present dimensions  $P_{captured}^{(j)} \approx -35.56$  dB. This value constitutes a good qualitative estimation of the SW coupling between adjacent feeds.

The aperture efficiency is found to be about 40%. The measured peak gain (28dB) is a bit lower than the expected

one; this is probably due to the losses in the feeding lines more than to the losses in the metal and in the dielectric of the antenna. The latter is predicted to be about 1.5 dB by the full wave analysis.

TABLE I. MEASURED ANTENNA PARAMETERS

Parameter	Value at 33.5 GHz
Input reflection coefficient	-25 dB
Coupling between ports	< -30 dB
Half-power beamwidth -azimuth	4.0°
Half-power beamwidth -elevation	4.1°
Side lobe level azimuth (H-plane)	-13 dB
Side lobe level elevation (E-plane)	-15 dB
Azimuth null deviation	0.8°
Elevation null deviation	0.5°
Cross-polar level $\Sigma$ beam	<-25 dB
Directivity $\Sigma$ beam	31.2 dB
Gain $\Sigma$ beam	28.0 dB
Aperture efficiency for the $\Sigma$ beam	40%

TABLE II. COMPARISON OF THE PROPOSED SOLUTION WITH OTHER LOW-PROFILE MONOPULSE ANTENNAS

Ref.	Antenna type	Band	Dir. [dB]	SLL [dB]	Null depth [dB]	Thickness
[7]	Microstrip array	Ku	24.5	-17.0	-30.0	0.024 $\lambda$
[13]	SIW slot array	Ku	25	-15	-20.0	0.081 $\lambda$
[14]	Annular slot array	X	22.0	-12.0	-30.0	0.700 $\lambda$
[15]	Radial line array	C	n/a	-18.0	-40.0	0.270 $\lambda$
[16]	RLSA	Ku	22.2	-14.5	-25.0	0.137 $\lambda$
[17]	Gap waveguide RLSA	W	32.3	-15.0	-40.0	0.240 $\lambda$
[18]	Radial LWA	K	26.0	-13.0	-22.0	0.085 $\lambda$
<b>This work</b>	Modulated MTS	Ka	31.2	-13.0	-22.0	0.074 $\lambda$

As discussed in the introduction, there have been extensive efforts to replace the often bulky monopulse reflectors and lenses with light-weight and low profile structures. The proposed design joins other low-profile solutions, which main characteristics are summarized in Table II. The annular slot and radial line arrays in [14] and [15], respectively, share with our antenna the use of a simple excitation scheme with an electrically thicker metallic parallel plates waveguides. The microstrip array in [4] employs a single-layer PCB, as our MTS, and represents the electrically thinnest structure. However, losses in the corporate feed network may impair its scalability for higher gains. A thicker double-layer SIW slot array was proposed in [13] for scanning, but its fabrication involves via drilling and an accurate substrate alignment. The most similar solutions compared to our MTS are the RLSAs in [16] and [17] and the radial LWA in [18]. Although our antenna is the thinnest among the latter, its main advantage is the possibility of providing very high directivities with a

scalable solution. It is to be observed that our solution provides the highest measured directivity among the selection of low-profile monopulse antennas in Table II (the values in [17] are simulated ones). Future developments should improve the depth of the nulls and the beam symmetry for the different  $\Delta$  beams.

## V. CONCLUSION

A monopulse radar Ka band antenna in metasurface printed technology has been presented. The structure has been designed by partitioning a circular aperture in four identical angular quadrants each of them radiating an independent broadside beam when excited by an individual monopole launcher. The four sub-apertures are virtually separated by properly designing the metasurface modulation. The design has been successfully tested by a measured prototype showing performance not at the same level of a monopulse reflector antenna or other types of solutions, but extremely satisfactory, considering the obtained advantages of flatness, simplicity and extreme low cost.

## VI. ACKNOWLEDGEMENTS

The work treated in this paper won the MBDA Two Stars Innovation Award 2019. The Authors wish to thank the MBDA international committee for the appreciation.

## REFERENCES

- [1] S. M. Sherman and D. K. Barton, "Monopulse Principles and Techniques". Norwood, MA, USA: Artech House, 1984.
- [2] W. Hu et al., "Liquid-crystal-based reflectarray antenna with electronically switchable monopulse patterns," *Electron. Lett.*, vol. 43, no. 14, p. 1, Jul. 2007.
- [3] L. Di Palma, A. Clemente, L. Dussopt, R. Sauleau, P. Potier and P. Pouliguen, "Radiation pattern synthesis for monopulse radar applications with a reconfigurable transmitarray antenna," *IEEE Trans. Antennas Propag.*, vol. 64, no. 9, pp. 4148–4154, Sept. 2016.
- [4] S. Raman, N. S. Barker, and G. M. Rebeiz, "A W-band dielectric-lens based integrated monopulse radar receiver," *IEEE Trans. Microw. Theory Techn.*, vol. 46, no. 12, pp. 2308–2316, Dec. 1998.
- [5] A. Lopez, "Monopulse networks for series feeding an array antenna," *IEEE Trans. Antennas Propag.*, vol. 16, no. 4, pp. 436–440, Jul. 1968.
- [6] Z.-W. Yu, G.-M. Wang, and C.-X. Zhang, "A broadband planar monopulse antenna array of C-band," *IEEE Antennas Wireless Propag. Lett.*, vol. 8, pp. 1325–1328, 2009.
- [7] H. Wang, D.-G. Fang, and X. G. Chen, "A compact single layer monopulse microstrip antenna array," *IEEE Trans. Antennas Propag.*, vol. 54, no. 2, pp. 503–509, Feb. 2006.
- [8] H. Wang, D.-G. Fang, and M. Li, "A single-channel microstrip electronic tracking antenna array with time sequence phase weighting on subarray," *IEEE Trans. Microw. Theory Techn.*, vol. 58, no. 2, pp. 253–258, Feb. 2010.
- [9] R. R. Kinsey, "An edge-slotted waveguide array with dual-plane monopulse," *IEEE Trans. Antennas Propag.*, vol. 47, no. 3, pp. 474–481, Mar. 1999.
- [10] Y. J. Cheng, W. Hong, and K. Wu, "Millimetre-wave monopulse antenna incorporating substrate integrated waveguide phase shifter," *IET Microw. Antennas Propag.*, vol. 2, no. 1, pp. 48–52, Feb. 2008.
- [11] B. Liu et al., "Substrate integrated waveguide (SIW) monopulse slot antenna array," *IEEE Trans. Antennas Propag.*, vol. 57, no. 1, pp. 275–279, Jan. 2009.
- [12] Y. J. Cheng, W. Hong, and K. Wu, "94 GHz substrate integrated monopulse antenna array," *IEEE Trans. Antennas Propag.*, vol. 60, no. 1, pp. 121–129, Jan. 2012.
- [13] K. Tekkouk, M. Ettore, L. Le Coq, and R. Sauleau, "SIW pillbox antenna for monopulse radar applications," *IEEE Trans. Antennas Propag.*, vol. 63, no. 9, pp. 3918–3927, Sep. 2015.
- [14] K. Kelly, and F. Goebels, "Annular slot monopulse antenna arrays," *IEEE Trans. Antennas Propag.*, vol. 12, no. 4, pp. 391–403, Jul. 1964.
- [15] H. Miyashita and T. Katagi, "Radial line planar monopulse antenna," *IEEE Trans. Antennas Propag.*, vol. 44, no. 8, pp. 1158–1165, Aug. 1996.
- [16] M. Sierra-Castañer, M. Sierra-Pérez, M. Vera-Isasa, and J. L. Fernandez-Jambrina, "Low-cost monopulse radial line slot antenna," *IEEE Trans. Antennas Propag.*, vol. 51, no. 2, pp. 256–263, Feb. 2003.
- [17] A. Tamayo-Domínguez, J. M. Fernández-González and M. Sierra-Castañer, "Monopulse RLSA antenna with gap-waveguide feeding network for space debris radar at 94 GHz," in *Proc. 48th Eur. Microw. Conf. (EuMC)*, pp. 400–403, Sep 2018.
- [18] D. Comite et al., "Design of a polarization-diverse planar leaky-wave antenna for broadside radiation," *IEEE Access*, vol. 7, pp. 28672–28683, 2019.
- [19] C. L. Holloway, E. F. Kuester, J. Gordon, J. O'Hara, J. Booth, and D. Smith "An overview of the theory and applications of metasurfaces: The two-dimensional equivalents of metamaterials." *IEEE Antennas Propag. Mag.*, vol. 54, no. 2, pp. 10–35, Apr. 2012.
- [20] C. Pfeiffer and A. Grbic, "Metamaterial Huygens' surfaces: Tailoring wave fronts with reflectionless sheets," *Phys. Rev. Lett.*, vol. 110, no. 19, p. 197401, May 2013.
- [21] M. Selvanayagam and G. Eleftheriades, "Discontinuous electromagnetic fields using orthogonal electric and magnetic currents for wavefront manipulation," *Opt. Expr.*, vol. 21, no. 12, pp. 14409–14429, Jun. 2013.
- [22] N. Yu, et al. "Flat optics: controlling wavefronts with optical antenna metasurfaces," *IEEE J. Sel. Topics Quantum Electron.* vol. 19, no. 3, May 2013, Art. no. 4700423.
- [23] S. Maci, G. Minatti, M. Casaletti, and M. Bosiljevac, "Metasurfing: Addressing waves on impenetrable metasurfaces," *IEEE Antennas Wireless Propag. Lett.*, vol. 10, pp. 1499–1502, 2011.
- [24] E. Martini and S. Maci, "Metasurface transformation theory," in *Transformation Electromagnetics and Metamaterials: Fundamental Principles and Applications*, D. H. Werner and D.-H. Kwon, Eds. Berlin: Springer, 2013.
- [25] C. Pfeiffer and A. Grbic, "A printed, broadband Luneburg lens antenna," *IEEE Trans. Antennas Propag.*, vol. 58, no. 9, pp. 3055–3059, Sep. 2010.
- [26] M. Bosiljevac, M. Casaletti, F. Caminita, Z. Sipus, and S. Maci, "Nonuniform metasurface Luneburg lens antenna design," *IEEE Trans. Antennas Propag.*, vol. 60, no. 9, pp. 4065–4073, Sep. 2012.
- [27] B. H. Fong, J. S. Colburn, J. J. Ottusch, J. L. Visher, and D. F. Sievenpiper, "Scalar and tensor holographic artificial impedance surfaces," *IEEE Trans. Antennas Propag.*, vol. 58, no. 10, pp. 3212–3221, Oct. 2010.
- [28] G. Minatti, F. Caminita, M. Casaletti, and S. Maci, "Spiral leaky-wave antennas based on modulated surface impedance," *IEEE Trans. Antennas Propag.*, vol. 59, no. 12, pp. 4436–4444, Dec. 2011.
- [29] G. Minatti, S. Maci, P. De Vita, A. Freni, and M. Sabbadini, "A circularly-polarized isoflux antenna based on anisotropic metasurface," *IEEE Trans. Antennas Propag.*, vol. 60, no. 11, pp. 4998–5009, Nov. 2012.
- [30] G. Minatti et al., "Modulated metasurface antennas for space: Synthesis, analysis and realizations," *IEEE Trans. Antennas Propag.*, vol. 63, no. 4, pp. 1288–1300, Apr. 2015.
- [31] M. Faenzi et al., "Metasurface antennas: New models, applications and realizations," *Sci. Rep.*, vol. 9, no. 1, p. 10178, Dec. 2019.
- [32] M. Mencagli, Jr., E. Martini, and S. Maci, "Surface wave dispersion for anisotropic metasurfaces constituted by elliptical patches," *IEEE Trans. Antennas Propag.*, vol. 63, no. 7, pp. 2992–3003, Jul. 2015
- [33] G. Minatti, F. Caminita, E. Martini, and S. Maci, "Flat optics for leaky waves on modulated metasurfaces: Adiabatic Floquet-wave analysis," *IEEE Trans. Antennas Propag.*, vol. 64, no. 9, pp. 3896–3906, Sep. 2016.
- [34] G. Minatti, F. Caminita, E. Martini, M. Sabbadini, and S. Maci, "Synthesis of modulated-metasurface antennas with amplitude, phase, and polarization control," *IEEE Trans. Antennas Propag.*, vol. 64, no. 9, pp. 3907–3919, Sep. 2016.
- [35] M. Faenzi, D. Gonzalez-Ovejero, and S. Maci, "Wideband active region metasurface antennas," *IEEE Trans. Antennas Propag.*, vol. 68, no. 3, pp. 1261–1272, Mar. 2020.
- [36] M. Faenzi, D. González-Ovejero, and S. Maci, "Flat Gain Broad-Band Metasurface Antennas," *IEEE Trans. Antennas Propag.*, vol. 69, no. 4, pp. 1942–1951, Apr. 2021.
- [37] D. González-Ovejero, G. Minatti, G. Chattopadhyay, and S. Maci, "Multibeam by metasurface antennas," *IEEE Trans. Antennas Propag.*, vol. 65, no. 6, pp. 2923–2930, Jun. 2017.

- [38] M. Bodehou, E. Martini, S. Maci, I. Huynen, and C. Craeye, "Multibeam and beam scanning with modulated metasurfaces". *IEEE Trans. Antennas Propag.*, vol. 68, no. 3, pp. 1273-1281, Mar. 2019.
- [39] M. Bodehou, C. Craeye, E. Martini, and I. Huynen, "A quasi-direct method for the surface impedance design of modulated metasurface antennas," *IEEE Trans. Antennas Propag.*, vol. 67, no. 1, pp. 24-36, Jan. 2018.
- [40] A. T. Pereda *et al.*, "Dual circularly polarized broadside beam metasurface antenna," *IEEE Trans. Antennas Propag.*, vol. 64, no. 7, pp. 2944-2953, Jul. 2016.
- [41] S. Pandi, C. A. Balanis and C. R. Birtcher, "Design of scalar impedance holographic metasurfaces for antenna beam formation with desired polarization," *IEEE Trans. Antennas Propag.*, vol. 63, no. 7, pp. 3016-3024, Jul. 2015
- [42] M. Mencagli, Jr., E. Martini, and S. Maci, "Transition function for closed-form representation of metasurface reactance," *IEEE Trans. Antennas Propag.*, vol. 64, no. 1, pp. 136-145, Jan. 2016.
- [43] F. Caminita and S. Maci, "New wine in old barrels: The use of the Oliner's method in metasurface antenna design," in *Proc. 44th Eur. Microw. Conf.*, Rome, Italy, Oct. 2014, pp. 437-439.
- [44] S. Maci and A. Cucini, "FSS-based EBG surface," in *Electromagnetic Metamaterials: Physics and Engineering Aspects*, N. Engheta and R. Ziolkowski Eds. Hoboken, NJ, USA: Wiley, 2006.
- [45] D. González-Ovejero and S. Maci, "Gaussian ring basis functions for the analysis of modulated metasurface antennas," *IEEE Trans. Antennas Propag.*, vol. 63, no. 9, pp. 3982-3993, Sep. 2015.
- [46] *CST Microwave Studio*, CST of America, Anaheim, CA, USA, 2018.



**Marco Faenzi** was born in Siena, Italy. He received the M.Sc. degree in telecommunications engineering (with a score of 110/110) from the Dept. of Information Engineering and Mathematics at University of Siena, Siena, Italy, in 2011. In the same year he won a Ph.D. position at the Dept. of Information Engineering and Mathematics at the University of Siena, focused on development of high gain apertures for space applications based on modulated metasurface structures realized by inductive or capacitive textures. He successively gained the Ph.D. degree in 2015. In 2015 he won a

co-financed Post-Doc grant in the Networking/Partnering Initiative framework by the European Space Agency and University of Siena. In 2016 he was co-recipient of the Sergei A. Schelkunoff Transactions Prize Paper Award by the IEEE Antennas and Propagation Society. From September 2018 to March 2020 he covered a position as Post-Doc researcher at the Institut d'Électronique et de Télécommunications de Rennes, University of Rennes 1, Rennes, France. In October 2021 he won a position as Researcher at Dept. of Information Engineering and Mathematics at the University of Siena. He has worked on metasurfaces holographic patterning for the optimization of aperture efficiency of dipoles excited planar resonator. During his Post-Doc activity he worked towards characterization, optimization and synthesis of modulated metasurface apertures for of multi-frequency and broadband operativity. He also worked toward application of metasurface technology for implementation multibeam and highly efficient monopulse apertures in linear and circular polarization.



**David González-Ovejero** (S'01-M'13-SM'17) was born in Gandía, Spain, in 1982. He received the M.S. degree in telecommunication engineering from the Universidad Politécnica de Valencia, Valencia, Spain, in 2005, and the Ph.D. degree in electrical engineering from the Université catholique de Louvain, Louvain-la-Neuve, Belgium, in 2012. From 2012 to 2014, he was a Research Associate with the University of Siena, Siena, Italy. In 2014, he joined the Jet Propulsion Laboratory, California Institute of Technology, Pasadena, CA, USA, where

he was a Marie Curie Post-Doctoral Fellow. Since 2016, he has been a tenured

researcher with the French National Center for Scientific Research (CNRS), Institut d'Électronique et des Technologies du numérique (IETR), Rennes, France. His current research interests include computational electromagnetics, large phased arrays, periodic structures, metasurfaces and submillimeter wave antennas. Dr. González-Ovejero was a recipient of a Marie Curie International Outgoing Fellowship from the European Commission 2013, the Sergei A. Schelkunoff Transactions Prize Paper Award from the IEEE Antennas and Propagation Society in 2016, the Best Paper Award in Antenna Design and Applications at the 11th European Conference on Antennas and Propagation in 2017, and the Best Paper Award in Electromagnetics at the 15th European Conference on Antennas and Propagation in 2021. Since 2019, he has been an Associate Editor of the IEEE TRANSACTIONS ON ANTENNAS AND PROPAGATION and the IEEE TRANSACTIONS ON TERAHERTZ SCIENCE AND TECHNOLOGY.



**Stefano MACI** (F04) received the Laurea Degree cum Laude at University of Florence in '87 and from '97 is a Professor at the University of Siena. Since 2000, he was member the Technical Advisory Board of 13 international conferences and member of the Review Board of 6 International Journals. In 2004-2007 he was WP leader of the Antenna Center of Excellence (ACE, FP6-EU) and in 2007-2010 he was International Coordinator of a 24-institution consortium of a Marie Curie Action (FP6). In 2004 he was the founder of the European School of Antennas (ESoA), a post graduate school that presently comprises 34 courses on Antennas, Propagation, Electromagnetic Theory, and Computational Electromagnetics and 150 teachers coming from 15 countries. Since 2004 is the Director of ESoA. Since 2010 he has been Principal Investigator of 6 cooperative projects financed by European Space Agency.

Professor Maci has been a former member of the AdCom of IEEE Antennas and Propagation Society (AP-S), associate editor of AP-Transaction, Chair of the Award Committee of IEEE AP-S, and member of the Board of Directors of the European Association on Antennas and Propagation (EurAAP). From 2008 to 2015 he has been Director of the PhD program in Information Engineering and Mathematics of University of Siena, and from 2013 to 2015 he was member of the first National Italian Committee for Qualification to Professor. He has been former member of the Antennas and Propagation Executive Board of the Institution of Engineering and Technology (IET, UK). He founded and has been former Director of the consortium FORESEEN, involving 48 European Institutions. He was the principal investigator of the Future Emerging Technology project "Nanoarchitectonics" of the 8<sup>th</sup> EU Framework program, and he is presently principal investigator of the EU program "Metamask". He was co-founder of 2 Spin-off Companies. He has been a Distinguished Lecturer of the IEEE Antennas and Propagation Society (AP-S), and EurAAP distinguished lecturer in the ambassador program. He was recipient of the EurAAP Award in 2014, of the IEEE Schelkunoff Transaction Prize in 2016, of the Chen-To Tai Distinguished Educator award in 2016, and of the URSI Dellinger Gold Medal in 2020. He has been TPC Chair of the METAMATERIAL 2020 conference and designed Chairperson of EuCAP 2023. In the last ten years he has been invited 25 times as key-note speaker in international conferences. He is President Elect of the IEEE Antennas and Propagation Society 2022.

The research interest of Prof Maci includes high-frequency and beam representation methods, computational electromagnetics, large phased arrays, planar antennas, reflector antennas and feeds, metamaterials and metasurfaces. His research activity is documented in 180 papers published in international journals, (among which 100 on IEEE journals), 10 book chapters, and about 450 papers in proceedings of international conferences. The papers he coauthored have been cited about 8300 times (h index 47, source: Google Scholar).